HHS Public Access

Author manuscript

Biomaterials. Author manuscript; available in PMC 2022 September 01.

Published in final edited form as:

Biomaterials. 2021 September ; 276: 121015. doi:10.1016/j.biomaterials.2021.121015.

Activation, Development, and Attenuation of Modeling- and Remodeling-Based Bone Formation in Adult Rats

Wenzheng Wang[1,2,+], **Wei-Ju Tseng**[1,+], **Hongbo Zhao**[1], **Tala Azar**[1], **Shaopeng Pei**[1], **Xi Jiang**[1], **Nathaniel Dyment**[1], **X. Sherry Liu**[1,*]

[1]McKay Orthopaedic Research Laboratory, Department of Orthopaedic Surgery, Perelman School of Medicine, University of Pennsylvania, Philadelphia, PA, United States

[2]Department of Orthopaedic Surgery, Union Hospital, Tongji Medical College, Huazhong University of Science and Technology, Wuhan, Hubei, China

Abstract

Activation of modeling-based bone formation (MBF - bone formation without prior activation of bone resorption), has been identified as an important mechanism by which anabolic agents, such as intermittent parathyroid hormone (PTH), rapidly elicit new bone formation. Using a novel cryohistology imaging platform, coupled with sequential multicolor fluorochrome injections, we demonstrated that MBF and remodeling-based bone formation (RBF) in the adult rat tibia model have similar contributions to trabecular bone homeostasis. PTH treatment resulted in a 2.4–4.9 fold greater bone formation rate over bone surface (BFR/BS) by RBF and a 4.3–8.5 fold greater BFR/BS by MBF in male, intact female, and ovariectomized female rats. Moreover, regardless of bone formation type, once a formation site is activated by PTH, mineral deposition continues throughout the entire treatment duration. Furthermore, by tracking the sequence of multicolor fluorochrome labels, we discovered that MBF, a highly efficient but often overlooked regenerative mechanism, is activated more rapidly but attenuated faster than RBF in response to PTH. This

[*]To whom correspondence should be addressed X. Sherry Liu, McKay Orthopaedic Research Laboratory, Department of Orthopaedic Surgery, University of Pennsylvania, 332A Stemmler Hall, 3450 Hamilton Walk, Philadelphia, PA 19104, USA, xiaoweil@pennmedicine.upenn.edu, Phone: 1-215-746-4668.

[+]These authors contribute equally to this study.

Authors' roles:

Wenzheng Wang: Data curation, Formal analysis, Investigation, Methodology, Writing - original draft. Wei-Ju Tseng: Data curation, Formal analysis, Investigation, Methodology, Writing - review & editing; .Hongbo Zhao: Data curation. Tala Azar: Data curation, Investigation, Writing - review & editing. Shaopeng Pei: Data curation, Formal analysis, Writing - review & editing. Xi Jiang: Methodology, Writing - review & editing. Nathaniel Dyment: Methodology, Investigation, Writing - review & editing. X. Sherry Liu: Conceptualization, Funding acquisition, Investigation, Supervision, Writing - original draft.

Conflict of Interest:

The authors declare that they have no conflict of interest.

Data availability

Some raw data and all processed data required to reproduce these findings are available to download from http://dx.doi.org/10.17632/z5vhcktxjx.1.

Other raw data required to reproduce these findings cannot be shared at this time due to technical or time limitations.

Declaration of interests

The authors declare that they have no known competing financial interests or personal relationships that could have appeared to influence the work reported in this paper.

suggests that MBF and RBF contribute differently to PTH's anabolic effect in rats: MBF has a greater contribution to the acute elevation in bone mass at the early stage of treatment while RBF contributes to the sustained treatment effect.

Keywords

Modeling- and remodeling-based bone formation; Bone histomorphometry; Anabolic treatments; Animal model; Osteoporosis

1. Introduction

The healthy skeleton continuously renews itself throughout life via the bone remodeling process where osteoclast resorption and osteoblast formation are closely coupled. Remodeling-based bone formation (RBF), which occurs over resorbed surfaces following osteoclast resorption (Figure 1A), plays a critical role in renewing bone tissue and maintaining the mechanical strength of the skeleton [1]. In contrast, an alternative pathway to elicit new bone formation is modeling-based bone formation (MBF), *i.e.*, bone formation without prior activation of bone resorption (Figure 1B) [2]. Compared to targeting RBF, stimulating MBF is potentially a more efficient regenerative mechanism and therapeutic target as it does not involve activation of osteoclasts to resorb bone matrix.

MBF, also referred to as minimodeling, was first identified in 1964 as a new bone packet with a smooth cement line without interruption of surrounding collagen fibers [3]. Previous studies suggested that MBF mainly occurs during growth and healing and is less commonly found in the adult skeleton [4–8]. Recently, the concept of MBF has received increased attention due to the discovery of its involvement in anabolic treatments for osteoporosis [6, 8–12]. Lindsay *et al.* reported that clinical treatment by teriparatide, intermittent injections of parathyroid hormone (PTH) 1–34, rapidly exerts its anabolic effect in one month by the activation of both RBF and MBF, where MBF may account for more than 30% of the bone gain induced by PTH [6]. Moreover, a study in rats and monkeys also reported that the anabolic effect of Romosozumab, a sclerostin neutralizing antibody (Scl-Ab), is primarily modeling-based, making MBF a promising target to treat osteoporosis [11, 13].

Despite the potent effect of anabolic agents on stimulating MBF and RBF, there are major challenges and limitations associated with these treatments. First, anabolic agents for osteoporosis can only be used for a short duration. For example, the FDA-recommended treatment duration for Scl-Ab is 12 months while the cumulative use of PTH and PTH related peptide (PTHrP) should not exceed 24 months during a patient's lifetime. Second, treatment efficacy attenuates with time. The bone forming effect of Scl-Ab is attenuated after 12 months [14, 15]. The efficacy of PTH also attenuates with time [16, 17]. However, osteoporosis in postmenopausal women and elderly men is a chronic condition. Therefore, there is a pressing need for novel therapeutic regimens to achieve sustained treatment efficacy and extend the duration of treatment. Currently, there is a significant knowledge gap regarding the activation and temporal development of bone tissue formed through RBF and MBF in response to treatments. It is critically important to advance our understanding of these two distinct bone formation mechanisms as they fundamentally influence the

efficiency of osteoporosis treatments. Moreover, quantitative data on the dynamics of MBF and RBF will also inform the design of mathematical models to better understand and predict bone formation in various disease conditions and in response to interventions [18–20].

Our current understanding of RBF and MBF mainly comes from clinical investigations, which typically involve one or two sets of fluorochrome injections and a transiliac bone biopsy taken from participants [6, 8, 10]. While these investigations provided essential knowledge on the involvement of RBF and MBF on human skeletal development, homeostasis, and response to osteoporosis treatments [6, 8–10], the nature of these clinical experimental designs restricts the investigation to a limited number of patients, fewer time points, and a shorter duration of observation. Studies on non-human primates also provided valuable insight into the kinetics of RBF and MBF in response to osteoporosis treatments [11–13]. However, the high cost, limited availability, and ethical challenges associated with non-human primates call for additional models of lower species for studies of RBF and MBF. To overcome these limitations, the first objective of the current study was to establish a rat model for the investigation of RBF and MBF by establishing their frequency and temporal dynamics in male, female, and ovariectomized (OVX) adult bone.

The second objective of the current study was to develop an imaging strategy to reliably identify RBF and MBF sites. Previous clinical investigations have utilized a quadruple tetracycline labeling method to identify and differentiate between RBF and MBF sites on undecalcified, thin plastic sections. This involves examinations on paired sections: fluorescent images of fluorochrome labels on one section, paired with brightfield and polarized images of osteons and cement lines on a second toluidine-blue stained section. In the current study, we adopt a multicolor fluorochrome labeling and cryohistology imaging strategy [21, 22], which involves multi-round imaging of the same cryosection before and after decalcification, to track the changes in RBF and MBF activity at a high temporal resolution (down to one week).

Furthermore, we chose the intermittent injection of PTH as a treatment strategy to test the activation, development, and attenuation of RBF and MBF because of its well-documented capacity to stimulate both RBF and MBF [6, 8, 10]. A third objective of this study was to compare differences between the dynamic response of RBF and MBF to both short-term (3-week) and long-term (9-week) PTH treatments. We hypothesize that RBF and MBF have different contributions to the early and long-term anabolic effect of PTH treatment.

2. Materials and Methods

2.1 Animals and treatment plans

All experiments were approved by the University of Pennsylvania’s Institutional Animal Care and Use Committee. A total of 54 Sprague Dawley rats were used in three sets of animal experiments.

First, an *in vivo* micro computed tomography (μCT) experiment was conducted to confirm the anabolic effect and establish the treatment dose and duration of PTH in ovariectomized

(OVX) rats. In pre-clinical studies, rats are typically treated with PTH at doses of 20–100 μg/kg/day. Due to the high accuracy and reproducibility of μCT and histomorphometry approaches used in this study, we first tested the lowest dose of 20 μg/kg/day in the *in vivo* μCT study. Twelve female rats received bilateral OVX surgery at the age of 16 weeks. Six weeks after surgery, PTH treatment (n=6) was administered to OVX rats by subcutaneous injections of 20 μg/kg/day (Human Recombinant PTH1–34, Bachem, Bubendorf, Switzerland) five times a week for three weeks. Similarly, age-matched, vehicle (VEH)-treated rats (n=6) received subcutaneous saline injections following the same injection schedule as rats in the PTH group.

The *in vivo* μCT study confirmed that a robust treatment response to PTH at 20 μg/kg/day for 3-weeks can be detected in OVX rats. Subsequently, PTH treatment at 20 μg/kg/day was administered to rats in two dynamic histomorphometry studies to (1) investigate the response of MBF and RBF to 3-week VEH and PTH treatments in adult male, female, and OVX rats and (2) investigate the response of MBF and RBF to 9-week PTH treatment in OVX rats. Twelve male and twenty-four female rats were used in the 3-week treatment study. Twelve female rats received bilateral OVX surgery at the age of 16 weeks. At 28 weeks of age, male, female intact, and OVX rats were randomly assigned to receive either VEH or PTH treatment (n=6/treatment group). Additionally, six OVX rats received PTH injections for 9 weeks.

All rats were housed in standard conditions in groups of three rats per cage, and all rats that underwent OVX surgery were separated to one rat per cage for one week following surgery to recover. Rats were euthanized at age 25–37 weeks.

2.2 In Vivo μCT Scans, Image Registration, and Bone Microstructural Analysis

μCT scans of the proximal tibia were performed on the VEH- and PTH-treated OVX rats (n=6/group) at weeks 0, 1, 2 and 3 using *in vivo* μCT (Scanco vivaCT40, Scanco Medical AG, Brüttisellen, Switzerland), as described in our previously published study [23]. Briefly, each rat was anesthetized (4/2% isoflurane) and the right tibia was fixed into a customized holder to ensure minimal motion. A 4.2-mm-thick segment of the proximal tibia (located 0.3 mm below the proximal growth plate) was scanned at 10.5 μm voxel size with a 200 ms integration time, 145 μA current, and 55 kVp energy. The average scan time per rat was approximately 20 minutes.

The sequential μCT scans were registered and aligned by using a mutual-information-based, landmark-initialized, rigid registration procedure based on open source software (National Library of Medicine Insight Segmentation and Registration Toolkit) [23, 24] to facilitate the selection of a consistent volume of interest (VOI). A 1.5-mm-thick trabecular VOI at week 3, located 2.6 mm distal to the growth plate, was identified in μCT images of scans from weeks 2, 1, and 0 (Figure 2A). Subsequently, the registered VOIs of trabecular bone were Gaussian filtered (sigma=1.2, support=2) and thresholded using a global threshold (corresponding to 544 mgHA/cm^3). Standard parameters of trabecular bone microstructure, including bone volume fraction (BV/TV) and trabecular thickness (Tb.Th), were quantified [25].

2.3 Multicolor fluorochrome injections and multiplexed cryohistology

Sequential fluorochrome labeling is a well-accepted technique for tracking the onset time and location of new bone deposition. According to our pilot study (Supplementary Materials), the calcium-binding fluorescent dyes actively bind to the mineralizing bone tissue up to 72 hours after injection (Supplementary Figure S1). To track the bone formation activity during the first day of treatment (day 0), the fluorochrome label was injected 2 days before the treatment started. Therefore, in the 3-week treatment study, each rat received a sequence of multicolor fluorochrome label injections including a subcutaneous injection of calcein (green, G, 15mg/kg), an intraperitoneal injection of alizarin complexone (red, R, 30mg/kg), and an intraperitoneal injection of tetracycline (yellow, Y, 30mg/kg) in the order of G-R-Y-G at days −2, 5, 12, 19 (initiation of PTH or VEH on day 0), followed by euthanasia at day 21. Similarly, in the 9-week treatment study, each rat received injections of multicolor fluorochrome labels in the sequence of G-R-Y-G at days −2, 19, 40, and 61 (initiation of PTH on day 0), followed by euthanasia at day 63.

After euthanasia, the left tibia was harvested and fixed in 4% paraformaldehyde (PFA) at 4 °C for 48 hours. Samples were then placed in a solution of 20% sucrose and 2% polyvinylpyrrolidone (PVP) for 48 hours, followed by cryoembedding in Tissue-Tek O.C.T. Compound (Sakura Finetek USA Inc, Torrance, CA) using liquid nitrogen. 8μm-thick sections were made from undecalcified specimens using cryofilm IIC tape (Section-Lab Co. Ltd., Hiroshima, Japan) as previously described [21]. Sections were attached to glass microscope slides using 1% chitosan adhesive, rehydrated 48 hours later in a 1x phosphate buffered saline (PBS) solution for 15 min, and then mounted with 50% glycerol. Mounted slides were scanned using the Axio Scan Z1 (Zeiss, Oberkochen, Germany) to obtain dark field and fluorescent images (Figure 1C-D and Figure 3A-C). After the first round of imaging, slides were submerged in 1x PBS to remove the cover slip. Slides were then submerged in Formical-2000™ decalcifier (StatLab, McKinney, TX) for 1 hour to completely decalcify the tissue section. Decalcified sections were remounted and observed under a polarizing microscope (Leica, Wetzlar, Germany) to visualize the cement line and collagen fiber alignment (Figure 1F & 1J).

2.4 Identification and histomorphometric measurements of RBF and MBF sites

Identification and histomorphometric measurements of RBF and MBF sites were performed in the secondary spongiosa located 1.0 – 2.5 mm below the growth plate (Figure 1D). Based on the first round of images of undecalcified sections, new bone formation sites were identified based on darkfield bone structure and multicolor fluorochrome labels (Figure 1E & 1I). Then, after sections were decalcified, the organization of the cement line and surrounding collagen fibers of each bone formation site were examined under the polarizing microscope (Figure 1F & 1J). The decalcification of the tissue section substantially improved the image quality of cement lines and collagen organization under the polarizing microscope (Supplementary Figure S2). Based on the two rounds of imaging and examinations, bone formation sites were designated as RBF if the underlying cement line was scalloped with interrupted collagen fiber alignment (Figure 1G-H), indicating prior osteoclast resorption, or as MBF if the underlying cement line was smooth with uniform collagen fiber alignment (Figure 1K-L), indicating *de novo* bone formation on quiescent

bone surface. Due to the anisotropic nature of the bone matrix, a polarizer rotation of 180° was required for a thorough examination of collagen alignment at each formation site. It should be noted that images from the polarized light microscope in Figure 1F and 1J only represent images taken at a single, fixed polarizer angle. The collagen organization of all bone packets were examined by a polarizer rotation of 180° and the observed results were shown as schematics in Figure 1H and 1L.

Subsequently, standard histomorphometric measurements were performed for RBF and MBF sites, respectively. Mineralizing surface (MS/BS, %) was defined as the percent of bone surface that displays multiple fluorochrome labels reflecting active minearlization over the total bone surface. Mineral apposition rate (MAR, μm/day) was measured by the distance between two fluorochrome labels, divided by the time interval between two label injections. Bone formation rate (BFR/BS, $\mu m^3/\mu m^2$/day or μm/day) was defined as the amount of newly formed bone tissue in unit time per unit bone surface. BRF/BS was calculated as MS/BS multiplied by MAR. The above measurements were defined and expressed according to recommendation from the American Society of Bone and Mineral Research (ASBMR) Histomorphometry Nomenclature Committee [26] and were measured using OsteoMeasure™ (OsteoMetrics, Atlanta, GA). All histomorphometric analysis was performed by a single reader (WW). To assess the precision and reproducibility of classification of MBF and RBF, a group of 3 readers (WW, TA, and SP) independently carried out the MBF and RBF site identification on 5 slides randomly selected from the PTH-treated OVX rats. The individual coefficient of variance (CV) was first calculated, and the precision error was defined as the root mean square average of the %CV (RMSCV) [27]. Next, the intraclass correlation coefficient (ICC) [28, 29] was calculated to indicate the absolute agreement between readers. Ranging from 0 to 1, ICC reflects the ratio of sample variance over the total variance, where an ICC close to 1 indicates a low variance resulting from different readers relative to the total variance, suggesting good repeatability between different readers.

Additionally, a pilot study was conducted to assess the agreement between 2D and 3D imaging methods on the identification of MBF and RBF sites (detailed methods described in Figure S3) on 5 bone samples randomly selected from the PTH-treated female intact rats. Briefly, a 3D image stack consisting of 46 2D images that are equivalent to 50 μm in depth was obtained. The fluorochrome labels and collagen fibers of the secondary spongiosa were imaged with spectral confocal and multiphoton microscopes (Leica TCS SP8, Leica Microsystems Inc.) while collagen fiber orientation was obtained using two-photon, second harmonic generation (SHG). The identification of MBF and RBF were performed on the first 2D image of the 3D image stack following the same standards that were used for the 2D cryosection. Next, each formation site was examined on 3D image stacks up to 50 μm. A MBF site shown on a 2D image might be identified as a RBF site based on 3D image stacks if scalloped cement lines with disrupted collagen fibers appeared on subsequent 2D images. Lastly, the precision error and the intraclass correlation coefficient (ICC) were calculated to indicate the agreement between 2D and 3D imaging methods.

2.5 Histomorphometric analysis of bone formation sites by activation time

In the groups that received PTH treatment, RBF and MBF were further stratified by their activation time based on the sequence of multicolor fluorochrome labels as shown in Figure 4A. In the 3-week PTH treatment study, four fluorochrome labels (G-R-Y-G) were injected right before weeks 0, 1, 2, and 3 (Figure 4A). A bone formation site that incorporated all four labels (G-R-Y-G) indicates that this site was active, or mineralizing, at week 0 (activated either before or at the onset of treatment). Similarly, a bone formation site that incorporated only three labels (R-Y-G) was activated during weeks 0–1 while a site with only two labels (Y-G) was activated during weeks 1–2 (Figure 4A). Mineral deposition continued until the end of the entire treatment duration if a formation site incorporated the last G label.

Similarly in the 9-week PTH treatment study, sites with all four labels (G-R-Y-G) were activated before or at the onset of treatment (week 0) and were active throughout the entire treatment duration (Figure 4E-4F). Sites with three labels (R-Y-G) were activated during weeks 0–3 and remained active until the end of treatment. Furthermore, sites with two labels (Y-G) would indicate any bone formation activated during weeks 3–6.

2.6 Histomorphometric analysis of mineral apposition during different treatment periods

Sequential fluorochrome injections allow the divison of formation sites by mineral labels into regions that are deposited during different periods of treatment. In the 3-week treatment study, the region between the first G label and the R label was deposited during weeks 0–1. The region between the R and Y labels was deposited during weeks 1–2, and the region between the Y label and the last G label was deposited during weeks 2–3 (Figure 5). Similarly, the regions between each two neighboring labels of G-R-Y-G in the 9-week treatment study were deposited during weeks 0–3 (1st G-R), weeks 3–6 (R-Y), and weeks 6–9 (Y-2nd G), respectively (Figure 6).

2.7 Statistical analysis

All statistical analyses were performed using NCSS Statistical System (NCSS, LLC, Kaysville, UT). Results were presented as boxplots with median and interquartile range (IQR; 25^{th} to 75^{th} percentile), and whiskers indicating maximum and minimum values. For longitudinal μCT image-based measurements, a mixed model was used to compare treatment groups over time. All comparisons were adjusted for baseline measures. In the presence of a significant interaction effect between time and treatment, individual comparisons were evaluated using Bonferroni *post hoc* corrections. A two-way analysis of variance (ANOVA) test was used to compare the effects of bone formation type and treatment on histomorphometric measurements. In the presence of a significant interaction effect, individual comparisons were evaluated using Bonferroni *post hoc* corrections. A one-way ANOVA with Bonferroni *post-hoc* tests was used to test the differences in histomorphometric variables of RBF and MBF between different activation times. For sites with a G-R-Y-G label in both the 3- and 9-week PTH treatment studies, a one-way ANOVA with Bonferroni *post-hoc* tests was performed to compare histomorphometric variables between different regions defined by the four mineral labels. Furthermore, the difference in

percentage changes of MBF and RBF was analyzed using paired students' t-tests. For all analyses, $p \leq 0.05$ was considered to indicate statistical significance.

3. Results

3.1 Three-week PTH treatment efficiently improved bone mass and thickness of trabeculae

Three-week PTH treatment in OVX rats led to a 29% and 33% increase in tibial BV/TV and Tb.Th, respectively (Figure 2B &2C). In contrast, the VEH group had no changes in BV/TV or Tb.Th after saline treatment. After treatment for two weeks, PTH led to substantially greater BV/TV and Tb.Th in PTH- *vs.* VEH-treated rats (Figure 2B &2C).

3.2. Multicolor fluorochrome injections labeled bone formation sites on the adult rat skeleton

In the 3-week VEH- and PTH-treated bone, an average of 95.1±6.2% of new bone formation sites could be identified as either RBF or MBF. However, due to the two-dimensional (2D) nature of the histological assessment, 4.9±6.2 % of new bone formation sites showed a limited area of interface with pre-existing bone, thus their formation type could not be reliably identified. Moreover, the percentage of unidentifiable bone formation sites increased to 29.1±5.6 % in the 9-week PTH-treated bone. This is due to the significantly greater thickness of new bone formation sites in the 9-week treatment group than in the 3-week treatment group, increasing the chance for the cement line of a formation site to fall outside of the 2D section plane (examples shown in Supplementary Figure S4).

Bone formation sites with distinct multicolor labels were more prevalent on PTH-treated than VEH-treated bone surfaces (Figure 3A-C). Moreover, once a bone formation site was activated by PTH, mineral deposition at the site continued throughout the entire treatment duration, as demonstrated by the presence of the G label injected 2 days before euthanasia as the last label on all bone formation sites in PTH-treated bone (indicated by thick arrows in Figure 3A-C). In contrast, the last fluorochrome label at a formation site on the VEH-treated bone is either R, Y, or G (indicated by dashed arrows in Figure 3A-C). This is because the natural bone formation process may stop at any time during the VEH treatment. A notable difference in rat bone from human biopsies is the rare presence of overflow MBF (oMBF) where new bone formation with a smooth underlying cement line extends beyond the boundary of the RBF [8, 10] (Supplementary Figure S5). Less than 1% of all formation sites were oMBF, in contrast to 17% oMBF as reported in humans [8, 10]. Detailed discussion of results related to oMBF can be found in the Supplementary Material (Figure S5).

3.3 Reproducibility and agreement on classification of MBF and RBF between different readers and between 2D and 3D imaging methods

Reproducibility tests were carried out by three independent readers based on randomly selected sections from PTH-treated OVX rats. The total number of bone formation sites identified by the three readers reached an ICC value (reflecting absolute agreement among three readers) of 0.99 and were associated with only 2.2% precision error, indicating excellent agreement on the identification of new bone formation sites. The precision error

of the number of RBF sites was 14.3% while that associated with MBF was 7.8%. The ICC of the number of RBF and MBF sites was 0.81 and 0.87, respectively, suggesting good repeatability and agreement between different readers.

A pilot study was conducted to assess agreement between 2D and 3D imaging methods on the identification of MBF and RBF sites based on randomly selected sections from PTH-treated female intact rats. The precision error of the number of RBF sites was 11.6% while that associated with MBF was 6.6 %. The ICC of the number of RBF and MBF sites was 0.90 and 0.97, respectively, suggesting excellent repeatability and agreement between 2D and 3D imaging methods. On average, 4.5 formation sites (4.1% of all sites) that were identified as MBF on a 2D section were discovered to have a scalloped cement line with disrupted collagen fibers on subsequent sections (an example shown in Figure S3). These overflow MBF (oMBF) sites were categorized as RBF sites on 3D imaging stacks. As a result, the precision error of the percent of MBF sites over all sites was 6.6% with an ICC of 0.80.

3.4. PTH exerts its anabolic action through a greater increase in MBF than RBF in the adult rat skeleton

Two-way ANOVA tests indicated significant effects of treatment, bone formation type, and their interactions on MS/BS and BFR/BS in all three rat cohorts. In VEH-treated rats, regardless of sex and estrogen status, there was minimal bone formation activity with only 2–5% MS/BS and low BFR/BS for both RBF and MBF (Figure 3D-F). No difference was found between the activity of RBF and MBF in VEH-treated male, female, or OVX rats, suggesting that both RBF and MBF contribute to skeletal homeostasis in the adult rat skeleton. In contrast, PTH treatment led to a greater increase in MBF than RBF in all three rat cohorts (Figure 3D-F). MS/BS by RBF was 3.0-, 3.4-, and 2.1-fold greater while MS/BS by MBF was 6.9-, 4.3-, and 3.3-fold greater in PTH *vs.* VEH-treated female, OVX, and male rats, respectively. Moreover, PTH also resulted in 3.1-, 4.9- and 2.4- fold greater BFR/BS by RBF and 8.5-, 7.2-, and 4.3- fold greater BFR/BS by MBF in female, OVX, and male rats, respectively (Figure 3D-F). A two-way ANOVA indicated no effect of interaction between treatment and bone formation type in MAR of male, female, or OVX rats. However, the effect of treatment was significant for MAR in all three groups of rats, suggesting that regardless of bone formation type, PTH-treated bone had greater MAR than VEH-treated bone. Moreover, a significant effect of bone formation type was found for MAR in OVX rats, indicating greater MAR at MBF *vs.* RBF sites regardless of treatment type (Figure 3D-F).

3.5. PTH treatment induces different activation dynamics between RBF and MBF

To establish the time course of activation and development of RBF and MBF during their early response to PTH treatment, we further stratified MBF and RBF by their activation times (Figure 4A). In intact females, 37%, 54%, and 9% of all MS/BS of RBF activated by PTH occurred at week 0, weeks 0–1, and weeks 1–2, respectively (Figure 4B). In contrast, 86%, 13%, and 1% of all MS/BS of MBF activated by PTH occurred at week 0, weeks 0–1, and weeks 1–2, respectively, suggesting that peak activation of MBF occurs earlier than that of RBF. Similar results were found for OVX and male rats (Figure 4C-D).

Since intact female, OVX, and male rats had similar outcomes in the 3-week treatment study, the 9-week PTH-treatment was only conducted on OVX rats to establish the long-term effect of PTH treatment on the activation of RBF and MBF in estrogen deficient, osteoporotic rats. Similar to the 3-week PTH-treated bone, once a bone formation site was activated by PTH, mineral deposition at the site continued throughout the entire treatment duration, as demonstrated by the presence of the G label that was injected two days before euthanasia as the last label on all bone formation sites. Surprisingly, we did not find any new bone formation sites with the sequence of Y-G labels. If there was any new bone formation initiated by PTH after the injection of the R label (week 3), the mineral apposition would continue throughout the entire treatment duration. Therefore a formation site activated after week 3 would incorporate the Y (week 6) and G (week 9) but not the R (week 3) label. The lack of Y-G labeled bone formation sites indicated that no new bone formation was activated between weeks 3 and 6 (Figure 4E-F). This further confirmed that new bone formation sites were primarily activated within the first 3 weeks of PTH treatment in adult rats. However, once a bone formation site is initiated by PTH, treatment beyond 3 weeks continues to stimulate new bone tissue deposition at ongoing formation sites.

3.6. PTH-induced mineral apposition levels at ongoing RBF and MBF sites are time dependent

To establish how the dynamics of mineral deposition change during PTH treatment, we measured the histomorphometric variables of sites activated at week 0 (G-R-Y-G) in both the 3-week and 9-week treatment studies of OVX rats because only these sites represent bone apposition throughout the entire treatment duration. In the 3-week treatment study, regions defined by two adjacent fluorochome labels (G-R, R-Y, and Y-G) at the G-R-Y-G sites were deposited during weeks 0–1, 1–2, and 2–3, respectively (Figure 5A). The MS/BS of RBF and MBF of weeks 1–2 was 58% and 49% greater and the MAR was 78% and 70% greater than those of weeks 0–1, respectively (Figure 5B-C). This resulted in a 1.6–1.8 fold greater BFR/BS by RBF and MBF in weeks 1–2 (Figure 5D). In weeks 2–3, the MS/BS of RBF and MBF were 64% and 58% greater compared to those of weeks 0–1, respectively (Figure 5B), while the MAR of RBF and MBF decreased to levels similar to those in weeks 0–1 (Figure 5C). As a result, BFR/BS of RBF and MBF during weeks 2–3 were 75–79% greater than those of weeks 0–1, but 31–35% lower than those of weeks 1–2. Furthermore, between RBF and MBF, there was no difference in percentage change of any histomorphometric variable during the 3-week treatment (Figure 5E-G).

In the 9-week treatment study, regions defined by two adjacent fluorochome labels (G-R, R-Y, and Y-G) at the G-R-Y-G sites were deposited during weeks 0–3, 3–6, and 6–9, respectively (Figure 6A). MS/BS of MBF or RBF did not differ between weeks 3–6 and 0–3. However, MS/BS of MBF and RBF during weeks 6–9 were 47% and 26% lower compared to weeks 0–3, respectively (Figure 6B). MAR of MBF and RBF both decreased by 28% during weeks 3–6 and 45–47% during weeks 6–9 compared to weeks 0–3 (Figure 6C). As a result, BFR/BS of RBF and MBF of weeks 3–6 were 32–34% lower than those of weeks 0–3. Moreover, BFR/BS of RBF and MBF during weeks 6–9 were 59% and 72% lower than those of weeks 0–3, respectively (Figure 6D). Altogether, this resulted in a higher percent

change of MS/BS and BFR/BS for MBF in weeks 6–9 from weeks 0–3, compared to that of RBF (Figure 6E-G).

4. Discussion

In this study, we developed a novel microscopic imaging platform and established an adult rat model for systematic investigation of the temporal development of RBF and MBF. By tracking the sequence of multicolor fluorochrome labels, we discovered that the activation of new RBF and MBF by PTH mainly occurs during the first two weeks of treatment where MBF is activated more rapidly than RBF. Moreover, regardless of the type of bone formation, once a formation site is activated by PTH, mineral deposition continues during the entire treatment duration. However, the rate of bone formation for both MBF and RBF peaks during the first two weeks of PTH treatment and then has a significant and continuous attenuation throughout the 9-week treatment duration.

Studies on adult humans suggested that bone modeling in the mature skeleton is intrinsically rare, accounting for 2–3% of the entire bone surface [1, 5]. In contrast, the occurrence of MBF in adult rat bone highly depends on skeletal site and animal age. A study conducted by Erben demonstrated that RBF predominates the turnover activity (70–91% of all formation sites) in vertebral trabecular bone from age 3 months to 12 months in female rats [30]. In contrast, a greater percentage of MBF was found in the proximal tibial metaphysis [30]. In the current study, we established the proximal tibial metaphysis region of 28-week-old rats as a model, which provides abundant sites of both RBF and MBF for investigation of their dynamics of activation and development. This was the first study that investigated the effect of sex and estrogen status on the contribution of MBF and RBF to skeletal homeostasis. Our results demonstrated that MBF and RBF in the adult rat tibia model have similar contributions to trabecular bone homeostasis regardless of sex and estrogen status.

Previous studies have reported that treatment of PTH in postmenopausal women and men is accompanied first by an increase in biochemical markers of bone formation and subsequently by markers of resorption [31–33]. In the current study, the majority of MBF was activated before the effect of the first fluorochrome label wore off, indicating the acute effect of PTH on the activation of new MBF. In contrast, more than half of RBF sites were activated a week after MBF sites. The faster activation of MBF than RBF observed in rats agrees well with the faster increase in markers of formation than those of resorption, which may be due to differences in the activation process between MBF and RBF. Since the initiation of RBF requires the recruitment of both osteoclasts and osteoblasts [34], RBF takes longer to activate. In contrast, MBF occurs on quiescent bone surfaces without prior activation of osteoclast resorption, thus requiring less time than RBF to be activated. Indeed, previous studies have demonstrated that PTH can increase bone formation by directly acting on osteoblast lineage cells to promote osteoblast differentiation, reduce osteoblast apoptosis, and reactivate quiescent bone lining cells [35–37]. Recent lineage tracing studies further demonstrated that both PTH and Scl-Ab promote the conversion of bone lining cells into osteoblasts [37, 38]. Therefore, osteoblasts elicited at MBF sites may have different recruitment mechanisms from those recruited to RBF sites, resulting in different activation

dynamics. Further investigations are needed to elucidate the differential cellular mechanisms behind the two distinct bone formation processes.

The absence of newly activated MBF or RBF sites after the first 3 weeks of PTH treatment suggested that sustained PTH treatment efficacy comes from continuous mineral deposition of the ongoing formation sites that were activated during the early stage of treatment. Once a new bone formation site was elicited by PTH, MAR and MS/BS rapidly increased in the second week compared to the first week, regardless of the type of bone formation. However, MAR and BFR/BS of active sites of MBF and RBF started to decrease during the third week of treatment and continued to decrease throughout the 9-week treatment duration. Taken together, the lack of activation of new bone formation sites beyond the early phase of PTH treatment and the attenuated mineral deposition at active formation sites leads to the attenuated treatment efficacy of PTH over time in rats.

Furthermore, our results suggested that MS/BS and BFR/BS at active MBF sites decreased more rapidly than those at RBF sites towards the end of the 9-week treatment. In a recent clinical study, Demspter *et al.* compared the percentage of ongoing bone formation stratified by formation type between 6- and 24-month PTH treatment. There were 2.81% and 2.01% RBF surfaces by 6- and 24-month PTH treatment while MBF surfaces were present at 0.84% and 0.34%, respectively. Although no significant change was detected between 6- and 24-month treatment due to the low subject number, the different decreases in MBF and RBF surfaces agree with our observation in rats. In addition to PTH, Scl-Ab exerts its anabolic effect primarily through MBF without affecting the RBF rate, as demonstrated by studies of 10-week Scl-Ab treatment on monkeys [11]. However, when the treatment duration was extended to 28 weeks, MBF became negligible while the treatment effect on RBF was sustained [13], suggesting that differences between the attenuation of MBF and RBF may not depend on the use of a specific anabolic agent or a specific animal species, but reflect inherent properties of MBF and RBF. We speculate that osteoblasts recruited at MBF and RBF sites may come from different pools of osteoprogenitors, which may lead to the fundamentally different cellular responses to anabolic treatments, resulting in the distinct activation and attenuation processes of RBF and MBF. Nevertheless, the detailed cellular mechanisms behind the RBF and MBF responses require further investigation.

This study has two important strengths. First, to our knowledge, this is the first study that longitudinally tracked the activation and development of individual RBF and MBF sites in response to anabolic treatments in rats at a high temporal resolution. It yielded important information on the two distinct bone formation types and provided critical insight to the future design of osteoporosis treatment strategies to leverage RBF or MBF to enhance treatment efficacy. Second, an important technical innovation of the current study is the use of a multicolor fluorochrome labeling and cryohistology imaging strategy [21], which involves multi-round imaging of the same cryosection before and after decalcification. This allows imaging of fluorochrome labels and collagen organization and allows for subsequent quantification on the same section. Previous studies of MBF and RBF on human and rodents were based on paired, MMA-embedded thin plastic sections [6, 8, 10, 11, 30, 39]. The associated embedding and sectioning processes are time consuming and/or require highly specialized equipment. The cryohistology method in the current study not only allows

for reliable identification of MBF and RBF, but also enables the future investigation of spatial-temporal coupling between bone cell activities and MBF/RBF through sequential immunohistochemistry (IHC) on a single cryosection [21].

This study also had some limitations. Due to the two-dimensional nature of cryosections, some of the formation sites may be erroneously interpreted as MBF occurring on a smooth surface based on the observed section plane, while a scalloped cement line may be present outside of the section plane. To overcome these limitations, a new imaging strategy using a confocal microscope coupled with second harmonic generation (SHG) was developed, which enabled the imaging of a 3D-stack of a thick bone segment to confirm the identification of MBF [40]. A pilot study was also performed and demonstrated a high consistency of identification of MBF and RBF between 2D and 3D imaging strategies. Indeed, due to the rare occurrences of oMBF in rat bone, only less than 5% of formation sites that were erroneously identified as MBF on a 2D image had scalloped cement lines present on adjacent images from a 3D image stack. Moreover, *in vivo* μCT imaging-based approaches have been used to identify bone resorption and formation in rats and mice in a 3D manner and could potentially be used to identify events of MBF and RBF [41–44]. Birkhold *et al.* for the first time assessed the spatio-temporal bone modeling and remodeling events on cortical bone surfaces in a mouse tibial loading model by using longitudinal *in vivo* μCT imaging with a time lapse of 5 days for 15 days [45]. Nevertheless, there were still challenges associated with *in vivo* μCT image-based approaches for accurate identification of MBF and RBF sites in the trabecular compartment in rodents, including the relatively low image resolution or voxel size (10 μm, equivalent to distance of mineral apposition in 7–10 days in rodents) and adverse effect of ionizing radiation on bone. Thus, future studies are required to further establish the *in vivo* μCT-based methodologies for quantitative evaluation of the dynamics of MBF and RBF in rodent trabecular bone. Second, the longer interval between fluorochrome label injections, especially in the 9-week treatment study (labels injected every 3 weeks), may lead to “label escape errors” where (1) a formation site may stop its activity before the injection of the next label or (2) a formation site may be activated between the injections of the two labels. However, the 9-week study indicated that once a formation site is activated by PTH, mineral deposition continues during the entire treatment duration, suggesting that no label escape errors due to the first scenario occur for these sites. Moreover, we only analyzed sites that were activated at the initiation of PTH treatment, minimizing both scenarios of label escape errors. Third, PTH treatment at 20 μg/kg/day was used in the current study. While this dose is towards the lower end of the doses typically used in rodent studies (20–100 μg/kg/day), it corresponds to 140 μg/day in humans (assuming a 60kg human, 7x/week injections, and based on a body surface conversion factor of 6.2 between humans and rats as recommended by the FDA [46]), which is beyond the recommended clinical dose (25–100 μg/day). A lower and more clinically relevant dose of PTH treatment needs to be thoroughly tested in the current rat model for future translational studies.

PTH was known as a pro-remodeling agent as the RBF activated by PTH accounts for 70% of new bone formation in human patients [6]. However, our study demonstrated that PTH activated significantly greater MBF than RBF in the adult rat tibia. These different treatment responses could partially result from the difference in the baseline MBF/RBF ratio between

primates and rats. MBF is intrinsically rare in the adult human and monkey skeletons [6–8, 13] where RBF predominates their skeletal turnover. In contrast, MBF and RBF contribute equally to skeletal homeostasis in the adult rat tibia. The increase in the ratio of MBF/RBF following PTH treatment in both human and rat skeletons suggests that PTH treatment is more efficient at activating MBF than RBF relative to the baseline MBF and RBF activity.

The current study focused on the response of RBF and MBF in the trabecular bone of the proximal tibia of the adult rat. Bone formation at the periosteal and endosteal cortex of the rat tibia metaphysis in response to treatments is confounded by the continuous endochondral ossification due to longitudinal growth [30, 47] (Supplementary Figure S6). On the other hand, longitudinal growth of the rat lumbar vertebrae is minimal at the age of 6 months and becomes undetectable beyond the age of 9 months [30]. Moreover, both the trabecular and cortical bone compartments of the adult rat lumbar vertebrae are predominated by RBF, which better mimics the physiology of the human skeleton. Therefore, we are interested in further establishing the treatment response of RBF and MBF in the rat lumbar vertebrae as well as their comparison to humans in our future studies. We expect that the rat lumbar vertebrae would be a cost-efficient and highly clinically relevant model for future investigations of therapeutic strategies that leverage MBF.

While the current study provided important knowledge on the activation, development, and attenuation of RBF and MBF in response to anabolic treatments, several fundamental questions remain to be answered. First, to date there is limited knowledge on the quality of bone tissue that results from MBF. Compared to RBF, a more naturally occurring formation type in the adult skeleton, the only reported difference in MBF is the shape of the cement line and alignment of underlying collagen fibers. It is unclear whether other aspects of tissue composition, structure, and mechanics of bone tissue from MBF differ from those of RBF, and whether such differences subsequently influence macro-scale bone fracture resistance. Second, data from our study demonstrated differences between MBF and RBF in their activation, development, and attenuation in response to PTH, suggesting that osteoblasts elicited at MBF sites may have different origins and recruitment dynamics from those at RBF. It will be of great interest to further elucidate the cellular mechanisms behind the RBF and MBF. Lastly, the knowledge and innovative research tools resulting from this study will lay the foundation for further investigation on the roles of MBF and RBF in other diseases and treatment conditions, such as bone formation around orthopaedic and dental implants, and in response to external loading.

In summary, this study established a novel cryohistology imaging platform, coupled with sequential multicolor fluorochrome injections, for tracking dynamic responses of RBF and MBF in adult rats. Our results demonstrated that MBF, a highly efficient but often overlooked regenerative mechanism, is activated more rapidly but is attenuated faster than RBF in response to PTH, suggesting that the two types of bone formation contribute differently to PTH's anabolic effect: MBF has a greater contribution to the acute elevation in bone mineral density (BMD) at the early stage of treatment while RBF contributes to the sustained treatment effect. The current study only represents the first attempt to fill the critical knowledge gap in our understanding of MBF and RBF. The established imaging platform and the rat model established here enable future investigations to

answer fundamental but clinically important questions regarding the long-term therapeutic implications of MBF and RBF, as well as the cellular mechanisms contributing to their differences.

Supplementary Material

Refer to Web version on PubMed Central for supplementary material.

Acknowledgements:

Research reported in this publication was supported by the Penn Center for Musculoskeletal Diseases (PCMD) NIH/NIAMS P30-AR069619, NIH/NIAMS T32-AR007132, NIH/NIAMS K01-AR066743 (to XSL), NIH/NIAMS R01-AR077598 (to XSL), and National Science Foundation (NSF) Award #1661858 (to XSL).

References:

1. Hattner R, Epker BN, and Frost HM, Suggested sequential mode of control of changes in cell behaviour in adult bone remodelling. Nature, 1965. 206(983): p. 489–90. [PubMed: 5319106]
2. Jee WS, Tian XY, and Setterberg RB, Cancellous bone minimodeling-based formation: a Frost, Takahashi legacy. J Musculoskelet Neuronal Interact, 2007. 7(3): p. 232–9. [PubMed: 17947806]
3. Takahashi H, Hattner R, Epker BN, and Frost HM, Evidence that bone resorption precedes formation at the cellular level. Henry Ford Hosp Med Bull, 1964. 12: p. 359–64.
4. Frost HM, Skeletal structural adaptations to mechanical usage (SATMU): 1. Redefining Wolff's law: the bone modeling problem. Anat Rec, 1990. 226(4): p. 403–13. [PubMed: 2184695]
5. Kobayashi S, Takahashi HE, Ito A, Saito N, Nawata M, Horiuchi H, Ohta H, Ito A, Iorio R, Yamamoto N, and Takaoka K, Trabecular minimodeling in human iliac bone. Bone, 2003. 32(2): p. 163–9. [PubMed: 12633788]
6. Lindsay R, Cosman F, Zhou H, Bostrom MP, Shen VW, Cruz JD, Nieves JW, and Dempster DW, A novel tetracycline labeling schedule for longitudinal evaluation of the short-term effects of anabolic therapy with a single iliac crest bone biopsy: early actions of teriparatide. J Bone Miner Res, 2006. 21(3): p. 366–73. [PubMed: 16491283]
7. Ma YL, Zeng Q, Donley DW, Ste-Marie LG, Gallagher JC, Dalsky GP, Marcus R, and Eriksen EF, Teriparatide increases bone formation in modeling and remodeling osteons and enhances IGF-II immunoreactivity in postmenopausal women with osteoporosis. J Bone Miner Res, 2006. 21(6): p. 855–64. [PubMed: 16753016]
8. Dempster DW, Zhou H, Recker RR, Brown JP, Recknor CP, Lewiecki EM, Miller PD, Rao SD, Kendler DL, Lindsay R, Krege JH, Alam J, Taylor KA, Melby TE, and Ruff VA, Remodeling- and Modeling-Based Bone Formation With Teriparatide Versus Denosumab: A Longitudinal Analysis From Baseline to 3 Months in the AVA Study. J Bone Miner Res, 2018. 33(2): p. 298–306. [PubMed: 29024120]
9. Hodsman AB and Steer BM, Early histomorphometric changes in response to parathyroid hormone therapy in osteoporosis: evidence for de novo bone formation on quiescent cancellous surfaces. Bone, 1993. 14(3): p. 523–7. [PubMed: 8363903]
10. Dempster DW, Zhou H, Ruff VA, Melby TE, Alam J, and Taylor KA, Longitudinal Effects of Teriparatide or Zoledronic Acid on Bone Modeling- and Remodeling-Based Formation in the SHOTZ Study. J Bone Miner Res, 2018. 33(4): p. 627–633. [PubMed: 29194749]
11. Ominsky MS, Niu QT, Li C, Li X, and Ke HZ, Tissue-level mechanisms responsible for the increase in bone formation and bone volume by sclerostin antibody. J Bone Miner Res, 2014. 29(6): p. 1424–30. [PubMed: 24967455]
12. Pennypacker BL, Chen CM, Zheng H, Shih MS, Belfast M, Samadfam R, and Duong LT, Inhibition of cathepsin K increases modeling-based bone formation, and improves cortical dimension and strength in adult ovariectomized monkeys. J Bone Miner Res, 2014. 29(8): p. 1847–58. [PubMed: 24591096]

13. Boyce RW, Niu QT, and Ominsky MS, Kinetic reconstruction reveals time-dependent effects of romosozumab on bone formation and osteoblast function in vertebral cancellous and cortical bone in cynomolgus monkeys. Bone, 2017. 101: p. 77–87. [PubMed: 28428078]
14. Cosman F, Crittenden DB, Adachi JD, Binkley N, Czerwinski E, Ferrari S, Hofbauer LC, Lau E, Lewiecki EM, Miyauchi A, Zerbini CA, Milmont CE, Chen L, Maddox J, Meisner PD, Libanati C, and Grauer A, Romosozumab Treatment in Postmenopausal Women with Osteoporosis. N Engl J Med, 2016. 375(16): p. 1532–1543. [PubMed: 27641143]
15. McClung MR, Brown JP, Diez-Perez A, Resch H, Caminis J, Meisner P, Bolognese MA, Goemaere S, Bone HG, Zanchetta JR, Maddox J, Bray S, and Grauer A, Effects of 24 Months of Treatment With Romosozumab Followed by 12 Months of Denosumab or Placebo in Postmenopausal Women With Low Bone Mineral Density: A Randomized, Double-Blind, Phase 2, Parallel Group Study. J Bone Miner Res, 2018. 33(8): p. 1397–1406. [PubMed: 29694685]
16. Cosman F, Eriksen EF, Recknor C, Miller PD, Guanabens N, Kasperk C, Papanastasiou P, Readie A, Rao H, Gasser JA, Bucci-Rechtweg C, and Boonen S, Effects of intravenous zoledronic acid plus subcutaneous teriparatide [rhPTH(1–34)] in postmenopausal osteoporosis. J Bone Miner Res, 2011. 26(3): p. 503–11. [PubMed: 20814967]
17. Cosman F, Nieves JW, Roimisher C, Neubort S, McMahon DJ, Dempster DW, and Lindsay R, Administration of teriparatide for four years cyclically compared to two years daily in treatment Naive and alendronate treated women. Bone, 2019. 120: p. 246–253. [PubMed: 30355512]
18. Giorgio I, Spagnuolo M, Andreaus U, Scerrato D, and Bersani AM, In-depth gaze at the astonishing mechanical behavior of bone: A review for designing bio-inspired hierarchical metamaterials. Math Mech Solids, 2020.
19. Jean-François G, A contribution to the mechanics and thermodynamics of surface growth. Application to bone external remodeling. Int J Eng Sci, 2012. 50(1): p. 166–91.
20. Lekszycki T and dell'Isola F, A mixture model with evolving mass densities for describing synthesis and resorption phenomena in bones reconstructed with bio-resorbable materials. J Appl Math Mech, 2012. 92(6): p. 426–44.
21. Dyment NA, Jiang X, Chen L, Hong SH, Adams DJ, Ackert-Bicknell C, Shin DG, and Rowe DW, High-Throughput, Multi-Image Cryohistology of Mineralized Tissues. J Vis Exp, 2016(115).
22. Kawamoto T and Shimizu M, A method for preparing 2- to 50-micron-thick fresh-frozen sections of large samples and undecalcified hard tissues. Histochem Cell Biol, 2000. 113(5): p. 331–9. [PubMed: 10883392]
23. Lan S, Luo S, Huh BK, Chandra A, Altman AR, Qin L, and Liu XS, 3D image registration is critical to ensure accurate detection of longitudinal changes in trabecular bone density, microstructure, and stiffness measurements in rat tibiae by in vivo micro computed tomography (μCT). Bone, 2013. 56(1): p. 83–90. [PubMed: 23727434]
24. Johnson HJ, McCormick M, and Ibanez L, The itk software guide third edition updated for itk version 4.5. Insight Software Consortium, Tech. rep, 2013.
25. Bouxsein ML, Boyd SK, Christiansen BA, Guldberg RE, Jepsen KJ, and Muller R, Guidelines for assessment of bone microstructure in rodents using micro-computed tomography. J Bone Miner Res, 2010. 25(7): p. 1468–86. [PubMed: 20533309]
26. Dempster DW, Compston JE, Drezner MK, Glorieux FH, Kanis JA, Malluche H, Meunier PJ, Ott SM, Recker RR, and Parfitt AM, Standardized nomenclature, symbols, and units for bone histomorphometry: a 2012 update of the report of the ASBMR Histomorphometry Nomenclature Committee. J Bone Miner Res, 2013. 28(1): p. 2–17. [PubMed: 23197339]
27. Zhao H, Chang CC, Liu Y, Yang Y, Tseng WJ, de Bakker CM, Chung R, Ghosh P, and Deng L, Reproducibility and Radiation Effect of High-Resolution In Vivo Micro Computed Tomography Imaging of the Mouse Lumbar Vertebra and Long Bone 2020. 48(1): p. 157–168.
28. Shrout PE and Fleiss JL, Intraclass correlations: uses in assessing rater reliability. Psychol Bull, 1979. 86(2): p. 420–8. [PubMed: 18839484]
29. Koo TK and Li MY, A Guideline of Selecting and Reporting Intraclass Correlation Coefficients for Reliability Research. J Chiropr Med, 2016. 15(2): p. 155–63. [PubMed: 27330520]
30. Erben RG, Trabecular and endocortical bone surfaces in the rat: modeling or remodeling? Anat Rec, 1996. 246(1): p. 39–46. [PubMed: 8876822]

31. Kurland ES, Cosman F, McMahon DJ, Rosen CJ, Lindsay R, and Bilezikian JP, Parathyroid hormone as a therapy for idiopathic osteoporosis in men: effects on bone mineral density and bone markers. J Clin Endocrinol Metab, 2000. 85(9): p. 3069–76. [PubMed: 10999788]
32. Hodsman AB, Hanley DA, Ettinger MP, Bolognese MA, Fox J, Metcalfe AJ, and Lindsay R, Efficacy and safety of human parathyroid hormone-(1–84) in increasing bone mineral density in postmenopausal osteoporosis. J Clin Endocrinol Metab, 2003. 88(11): p. 5212–20. [PubMed: 14602752]
33. Lindsay R, Nieves J, Formica C, Henneman E, Woelfert L, Shen V, Dempster D, and Cosman F, Randomised controlled study of effect of parathyroid hormone on vertebral-bone mass and fracture incidence among postmenopausal women on oestrogen with osteoporosis. Lancet, 1997. 350(9077): p. 550–5. [PubMed: 9284777]
34. Langdahl B, Ferrari S, and Dempster DW, Bone modeling and remodeling: potential as therapeutic targets for the treatment of osteoporosis. Ther Adv Musculoskelet Dis, 2016. 8(6): p. 225–235. [PubMed: 28255336]
35. Jilka RL, Molecular and cellular mechanisms of the anabolic effect of intermittent PTH. Bone, 2007. 40(6): p. 1434–46. [PubMed: 17517365]
36. Kousteni S and Bilezikian JP, The cell biology of parathyroid hormone in osteoblasts. Curr Osteoporos Rep, 2008. 6(2): p. 72–6. [PubMed: 18778567]
37. Kim SW, Pajevic PD, Selig M, Barry KJ, Yang JY, Shin CS, Baek WY, Kim JE, and Kronenberg HM, Intermittent parathyroid hormone administration converts quiescent lining cells to active osteoblasts. J Bone Miner Res, 2012. 27(10): p. 2075–84. [PubMed: 22623172]
38. Kim SW, Lu Y, Williams EA, Lai F, Lee JY, Enishi T, Balani DH, Ominsky MS, Ke HZ, Kronenberg HM, and Wein MN, Sclerostin Antibody Administration Converts Bone Lining Cells Into Active Osteoblasts. J Bone Miner Res, 2017. 32(5): p. 892–901. [PubMed: 27862326]
39. Cui L, Ma YF, Yao W, Zhou H, Setterberg RB, Liang TC, and Jee WS, Cancellous bone of aged rats maintains its capacity to respond vigorously to the anabolic effects of prostaglandin E2 by modeling-dependent bone gain. J Bone Miner Metab, 2001. 19(1): p. 29–37. [PubMed: 11156470]
40. Tseng WJ, Wang W, Zhao H, Bennett A, Mariani L, Li Y, Dyment NA, Kim DG, Turner K, and Liu XS Differences in material properties of trabecular bone tissue from modeling- and remodeling-based bone formation in rats in 2020 Annual Meeting of Orthopaedic Research Society. 2020.
41. Birkhold AI, Razi H, Duda GN, Weinkamer R, Checa S, and Willie BM, The influence of age on adaptive bone formation and bone resorption. Biomaterials, 2014. 35(34): p. 9290–301. [PubMed: 25128376]
42. De Bakker CM, Altman AR, Tseng WJ, Tribble MB, Li C, Chandra A, Qin L, and Liu XS, μCT-based, in vivo dynamic bone histomorphometry allows 3D evaluation of the early responses of bone resorption and formation to PTH and alendronate combination therapy. Bone, 2015. 73: p. 198–207. [PubMed: 25554598]
43. Lambers FM, Schulte FA, Kuhn G, Webster DJ, and Muller R, Mouse tail vertebrae adapt to cyclic mechanical loading by increasing bone formation rate and decreasing bone resorption rate as shown by time-lapsed in vivo imaging of dynamic bone morphometry. Bone, 2011. 49(6): p. 1340–50. [PubMed: 21964411]
44. Schulte FA, Lambers FM, Kuhn G, and Muller R, In vivo micro-computed tomography allows direct three-dimensional quantification of both bone formation and bone resorption parameters using time-lapsed imaging. Bone, 2011. 48(3): p. 433–42. [PubMed: 20950723]
45. Birkhold AI, Razi H, Weinkamer R, Duda GN, Checa S, and Willie BM, Monitoring in vivo (re)modeling: a computational approach using 4D microCT data to quantify bone surface movements. Bone, 2015. 75: p. 210–21. [PubMed: 25746796]
46. Estimating the maximum safe starting dose in initial clinical trials for therapeutics in adult healthy volunteers, U.S. F.D.A., Editor. 2005.
47. Altman AR, Tseng WJ, de Bakker CM, Chandra A, Lan S, Huh BK, Luo S, Leonard M, Qin L, and Liu XS, Quantification of skeletal growth, modeling, and remodeling by in vivo micro computed tomography. Bone, 2015. 81: p. 370–9. [PubMed: 26254742]

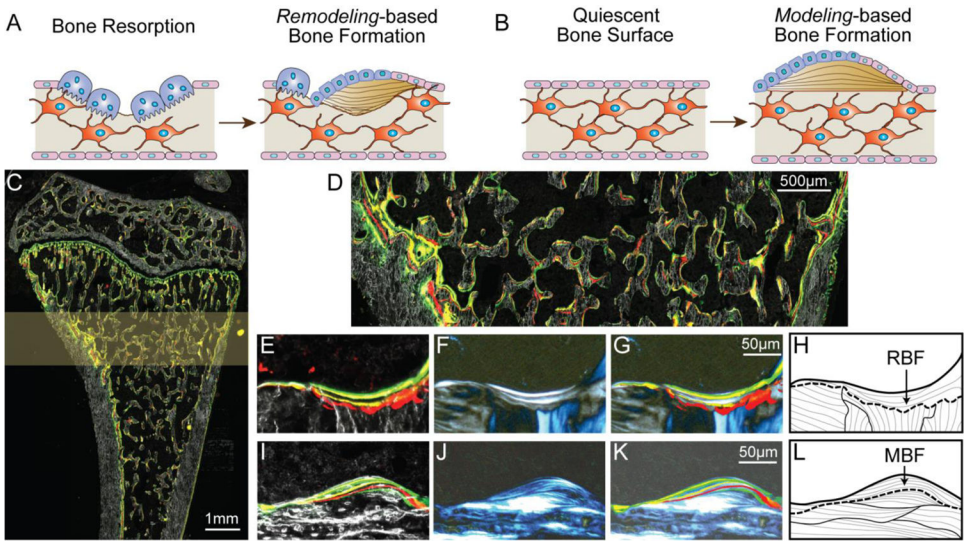

Figure 1.

Identification of RBF and MBF on the rat proximal tibia. (A-B) Schematics of (A) RBF and (B) MBF. (C) A representative image of an undecalcified cryosection of the rat proximal tibia with multiple fluorochrome labels under fluorescent light. (D) The secondary spongiosa located 1.0 – 2.5 mm below the growth plate was selected as the region of interest (highlighted in C) for further analysis. Representative (E-H) RBF and (I-L) MBF sites shown by (E&I) dark field and fluorescent light microscopy, (F&J) polarizing microscopy, and (G&K) overlaid images of E-F and I-J, respectively. It should be noted that images in 1F and 1J represented images taken at one fixed polarizer angle. The collagen organization of all bone packets was examined by a polarizer rotation of 180° and the observed results were shown as schematics in 1H and 1L. (G-H) RBF sites were identified by (E) scalloped cement lines with (F) interrupted collagen fiber alignment while (K-L) MBF sites were identified by (I) smooth cement lines and (J) uniform collagen fiber alignment.

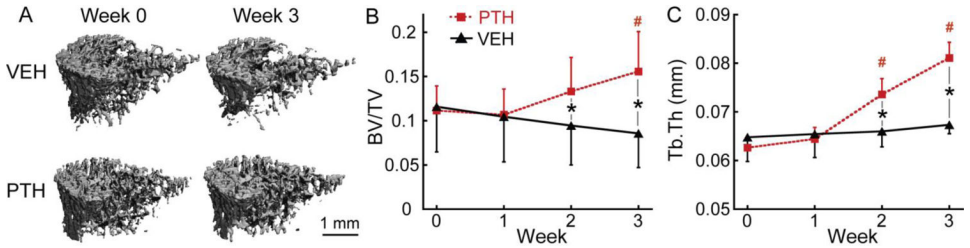

Figure 2.

μCT image analysis of tibial trabecular bone in response to VEH and PTH treatment in OVX rats. (A) Representative 3D renderings of the proximal tibia of a VEH- and PTH-treated rat at weeks 0 and 3. (B-C) Changes in (B) BV/TV and (C) Tb.Th of tibial trabecular bone in PTH and VEH groups. # indicates a significant difference from week 0 in the PTH group ($p<0.05$). * indicates a significant difference between the PTH and VEH groups ($p<0.05$).

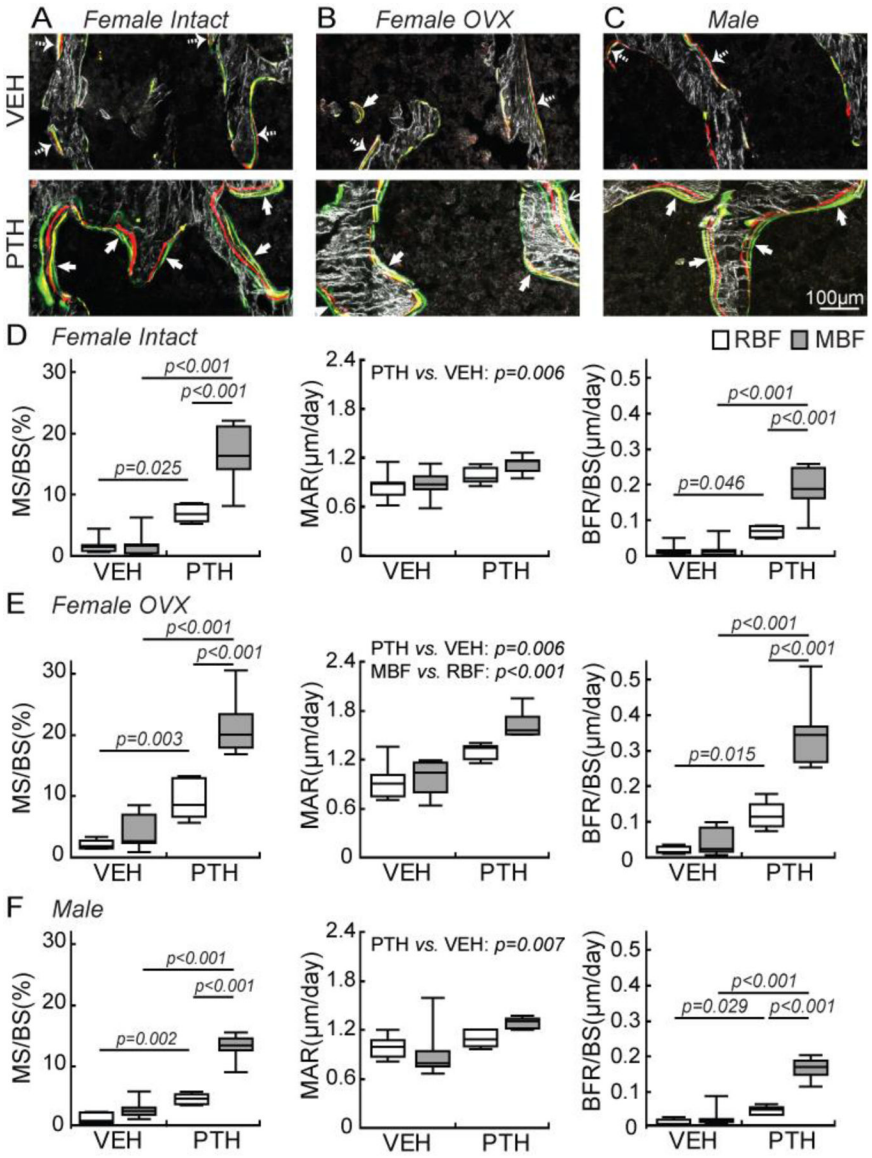

Figure 3.

Histomorphometric analysis of RBF and MBF in response to VEH and PTH treatments in female intact, female OVX, and male rats. (A-C) Representative images of new bone formation sites with a calcein label (thick arrow) or a random label (dashed arrow) as the last mineralization label in (A) female intact, (B) female OVX, and (C) male rats, respectively. (D-F) MS/BS, MAR, and BFR/BS of MBF and RBF in response to VEH and PTH in (D) female intact, (E) female OVX, and (F) male rats, respectively. Using two-way ANOVAs, individual comparisons were made for MS/BS and BFR/BS of all rat groups where significant interaction effects between formation type and treatment ($p<0.05$) were found. Due to the lack of interaction effect ($p>0.05$), group-wise comparisons were not made for MAR of any rat group.

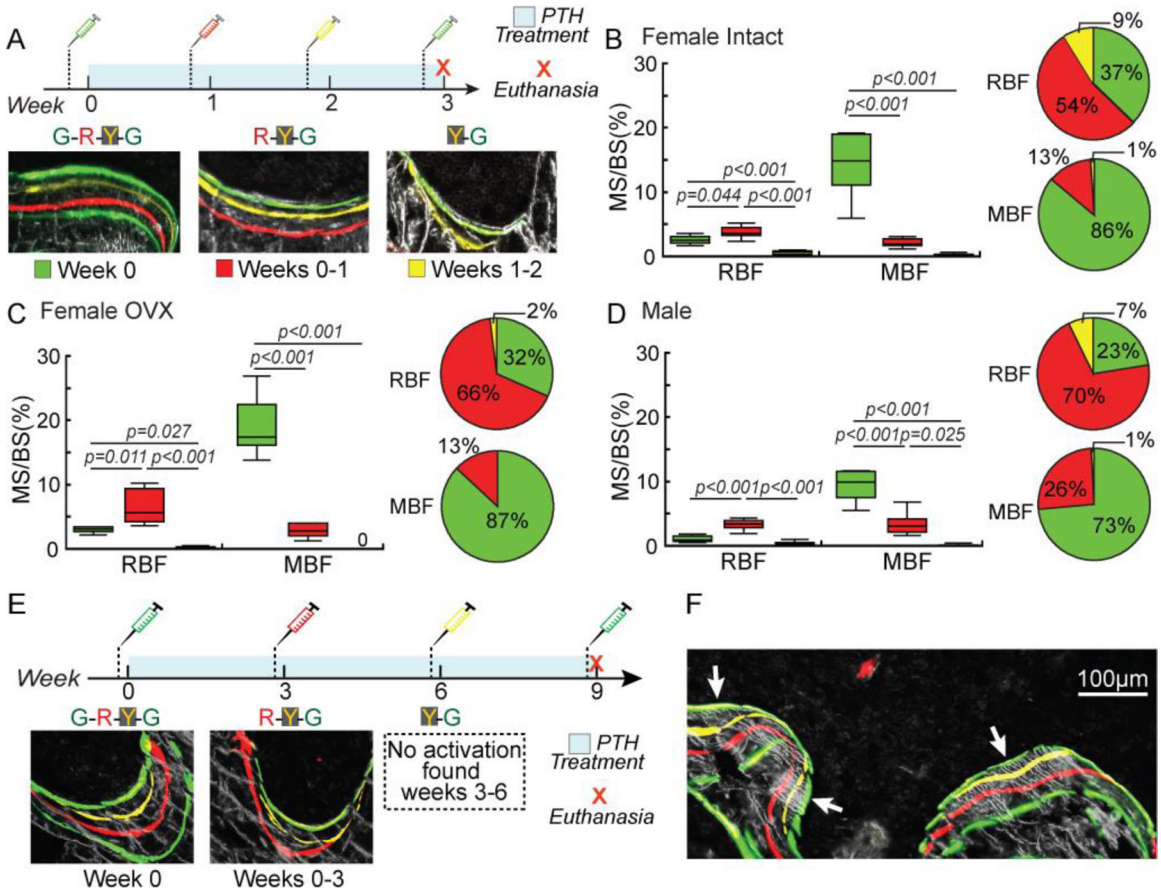

Figure 4.

Histomorphometric analysis of RBF and MBF stratified by activation time in PTH-treated rats. (A) Fluorochrome injection plan and representative bone formation sites stratified by activation time in the 3-week PTH treatment group. (B-D) MS/BS and BFR/BS of MBF and RBF stratified by activation time in (B) female intact, (C) female OVX, and (D) male rats treated with PTH. *: p≤0.05 by one-way ANOVA with Bonferroni corrections. (E) Fluorochrome injection plan and representative bone formation sites stratified by activation time in the 9-week PTH treatment group. (F) A representative image of new bone formation sites with a calcein label (thick arrow) as the last mineralization label.

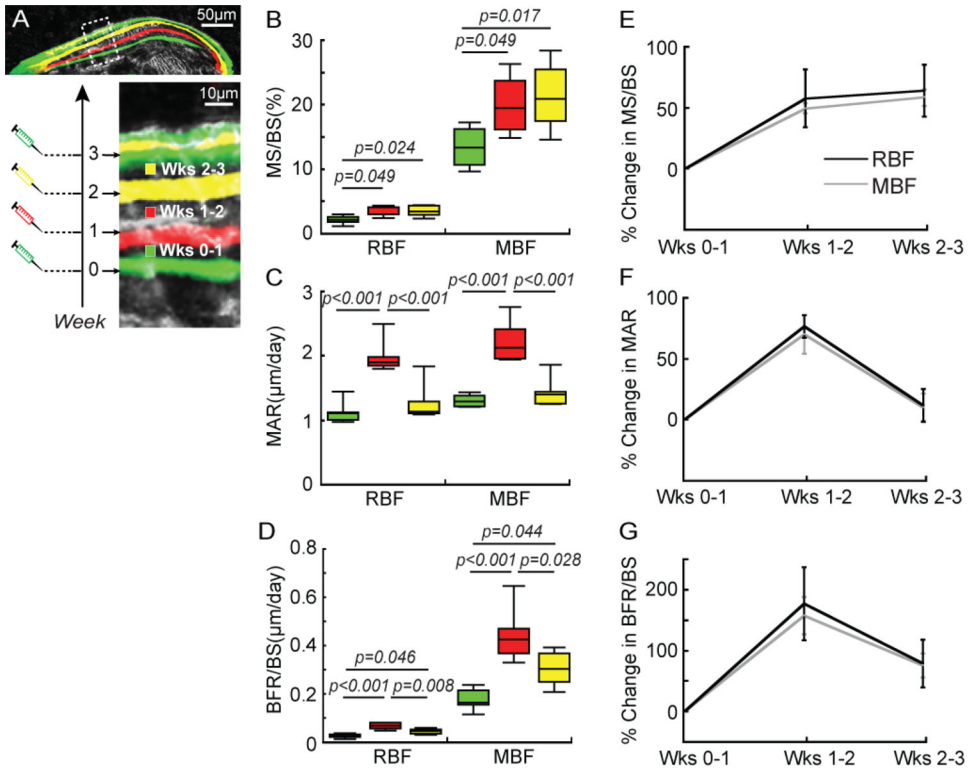

Figure 5.

Histomorphometric analysis of mineral apposition during different treatment durations (weeks 0–1, 1–2, and 2–3) in OVX rats. (A) A representative image showing the division of a bone formation site by mineral labels in an OVX rat that underwent 3 weeks of PTH treatment. Fluorochrome labels divided the bone formation site that was activated at week 0 into three regions. Each region was deposited during a specific time frame (the first, second, and third week of PTH treatment). (B-D) MS/BS, MAR, and BFR/BS of MBF and RBF and (E-G) their percentage change during each week of treatment.

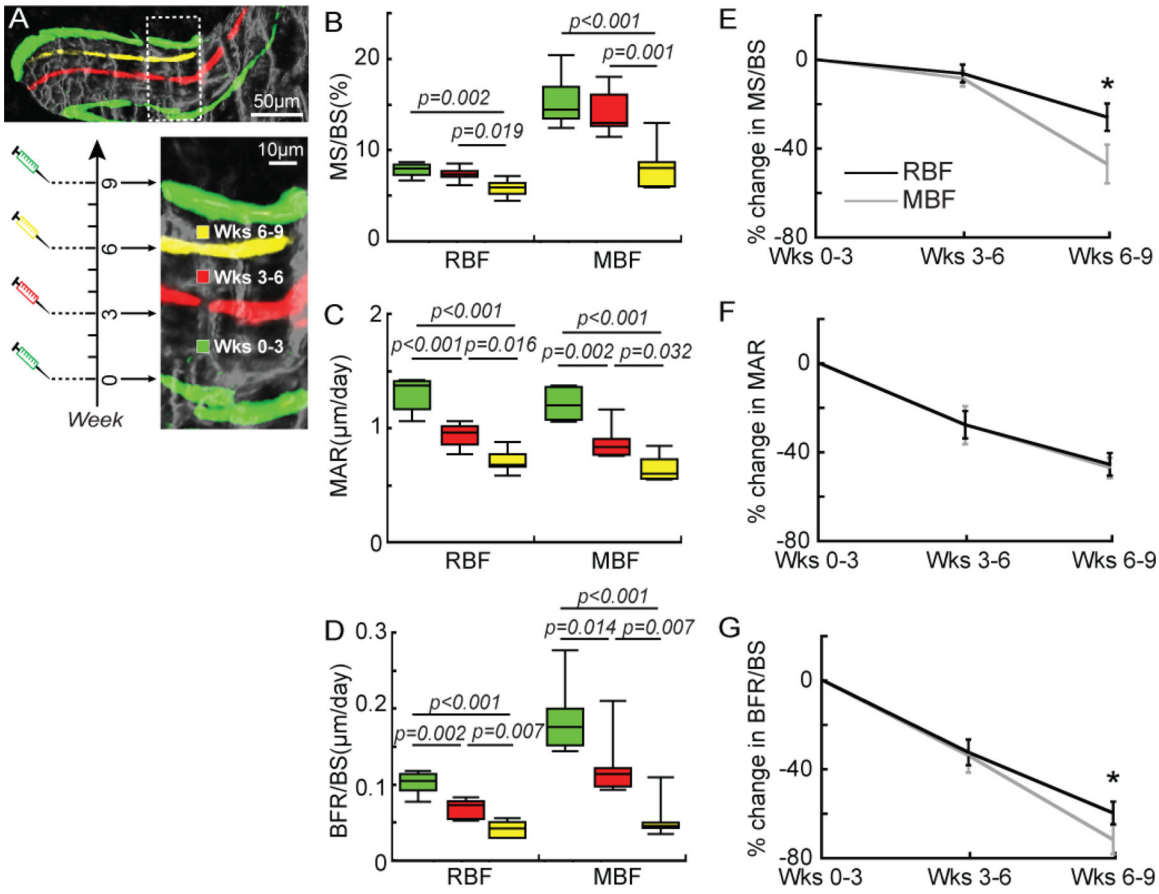

Figure 6.

Histomorphometric analysis of mineral apposition during different treatment durations (weeks 0–3, 3–6, and 6–9) in OVX rats. (A) A representative image showing the division of a bone formation site by mineral labels in an OVX rat that underwent 9 weeks of PTH treatment. Fluorochrome labels divided the bone formation site that was activated at week 0 (G-R-Y-G sites) into three regions. Each region was deposited during a specific time frame (weeks 0–3, 3–6, and 6–9 of PTH treatment). (B-D) MS/BS, MAR, and BFR/BS of MBF and RBF and (E-G) their percentage change during each week of treatment. * $p<0.05$ between MBF and RBF.

Table 1.

Reproducibility assessment of identification of MBF and RBF sites between different readers: root mean square of standard deviation (RMSSD), root mean square of percent coefficient of variance (RMS%CV), and intraclass correlation coefficient (ICC) for absolute agreement.

	Mean	RMSSD	RMS%CV	Absolute ICC
No. of total formation sites	46.5	1.0	2.2%	0.99
No. of RBF sites	16.5	2.4	14.3%	0.81
No. of MBF sites	30.0	2.7	7.8%	0.87

Table 2.

Reproducibility assessment of identification of MBF and RBF sites between 2D and 3D imaging methods: root mean square of standard deviation (RMSSD), root mean square of percent coefficient of variance (RMS%CV), and intraclass correlation coefficient (ICC) for absolute agreement.

	Mean	RMSSD	RMS%CV	Absolute ICC
No. of RBF sites	41.9	4.5	11.6%	0.90
No. of MBF sites	79.9	4.5	6.6%	0.97
% of MBF over all sites	64.8%	0.041%	6.6%	0.80